Chemical Engineering Journal 507 (2025) 160765

Contents lists available at ScienceDirect

Chemical Engineering Journal

journal homepage: www.elsevier.com/locate/cej

Rapid Joule heating processing of nickel-based flexible supercapacitors

Ye Tian [a,b], Shuonan Wang [c], Ning Liu [a,b], Qian Xue [b], Xueqiang Qi [d], Hao Liu [a,*], Andreu Cabot [b,e,*], Libing Liao [c,*]

[a] School of Science, China University of Geosciences, Beijing 100083, China
[b] Catalonia Institute for Energy Research – IREC, Sant Adrià de Besòs, Barcelona 08930, Spain
[c] Engineering Research Center of Ministry of Education for Geological Carbon Storage and Low Carbon Utilization of Resources, Beijing Key Laboratory of Materials Utilization of Nonmetallic Minerals and Solid Wastes, School of Materials Science and Technology, China University of Geosciences (Beijing), Beijing 100083, China
[d] College of Chemistry and Chemical Engineering, Chongqing University of Technology, Chongqing 400054, China
[e] Catalan Institution for Research and Advanced Studies – ICREA, Pg. Lluís Companys 23, Barcelona 08010, Spain

ARTICLE INFO

Keywords:
Rapid Joule heating processing
Nickle sulfide
Nickle oxide
Heterostructure
Hybrid asymmetric supercapacitor

ABSTRACT

In this study, an ultrafast Joule heating method is employed to efficiently synthesize nickel sulfide and nickel oxide nanoparticles on buckypaper (Ni_3S_2-NiO@BP) as high-performance supercapacitor electrode materials. The thermal shock effect was tuned by adjusting the temperature of Joule heat through voltage regulation. The resulting composite material exhibits battery-like energy storage kinetics, boasting a specific capacity of 2278F g^{-1} at a current density of 1 A g^{-1}. Ex-situ X-ray diffraction and Raman spectroscopy measurements showed that Ni_3S_2-NiO gradually transforms into $Ni(OH)_2$ during cycling, and then to highly reactive NiOOH. Density functional theory (DFT) calculations confirm the enhanced conductivity and OH^- adsorption of the heterogeneous structures. Furthermore, flexible hybrid asymmetric supercapacitors assembled from these electrodes exhibit a high energy density of 71.55 Wh kg^{-1} with a power density of 1124.8 W kg^{-1}, and stable electrochemical performance even under varying bending angles. The efficient synthesis approach presented here offers new insights into the rational design and engineering of electrode materials for high-performance, flexible supercapacitors.

1. 1.Introduction

Supercapacitors bridge the gap between high-energy–density batteries and high-power-density conventional capacitors, offering rapid charge–discharge rates, exceptional specific capacitance, superior power density, and ultra-long cycle life. These qualities make them highly promising for applications in electric vehicles, backup power supplies, and particularly wearable electronic devices [1–3]. In this last direction, flexible supercapacitors that meet both performance and mechanical demands are essentia. In this context, composite electrodes with a high load of active material on a porous structure that enables both high electronic and ionic conductivities while accommodating volume changes are needed. However, traditional slurry coating methods for electrode fabrication, which rely on solid current collector supports, present limitations. These include restricted electrode porosity, limited flexibility of the relatively thick metal supports that enable proper processing, and reduced energy density due to the addition of binders necessary for particle adhesion. These binders not only add inactive weight and volume but also hinder electron and ion transport both at the redox particle surface and across the electrode, reducing electrolyte penetration and, consequently, redox activity [4–8]. Additionally, slurry-based processes often require toxic organic solvents, posing environmental and health concerns [9].

To address these limitations, cost-effective strategies for depositing active materials on highly porous conductive networks are required. One approach involves impregnating the porous network with metal salts, facilitating effective ion infiltration throughout the structure, and subsequently annealing the produced material to fixate and crystallize the desired phase [10]. However, this strategy is often time-consuming and energy-intensive, and can lead to uncontrolled growth and aggregation of the active phase, diminishing redox performance. In terms of electrode materials, Ni-based compounds are particularly promising as the redox-active phase for their rich oxidation states, high theoretical capacity, and low toxicity [11,12]. Among Ni compounds, NiO offers the lowest density and cost, while incorporating sulfur can enhance electrochemical activity and redox reaction rates due to the higher electrical

* Corresponding authors at: Catalonia Institute for Energy Research – IREC, Sant Adrià de Besòs, Barcelona 08930, Spain.
E-mail addresses: liuhao1398@cugb.edu.cn (H. Liu), andreucabot@gmail.com (A. Cabot), lbliao@cugb.edu.cn (L. Liao).

https://doi.org/10.1016/j.cej.2025.160765
Received 19 December 2024; Received in revised form 25 January 2025; Accepted 16 February 2025
Available online 17 February 2025
1385-8947/© 2025 Elsevier B.V. All rights are reserved, including those for text and data mining, AI training, and similar technologies.

conductivity of the sulfide and the higher electronegativity of sulfur that promotes electron transfer. For the conductive matrix, buckypaper (BP), a multi-walled carbon nanotube material, provides an ideal substrate due to its exceptional electrical conductivity, structural stability, and large surface area for loading large amounts of active electrode materials to meet the design requirements of one-piece flexible electrode materials [13–16].

In this study, we propose a novel method for processing supercapacitor electrodes using energy-efficient, ultrarapid Joule thermal shock. Joule heating, which generates heat by passing an electric current through a material, offers several advantages: rapid processing time, elimination of solvents and catalysts, and the ability to act directly on the carbon matrix without requiring specialized gas environments [17–20]. Using this technique, herein we produce nickel sulfide-nickel oxide heterostructured nanoparticles on BP as electrode materials for flexible supercapacitors, demonstrating the potential of this ultrafast processing approach to enhance supercapacitor performance.

2. Experimental

2.1. Synthesis of Ni_3S_2-NiO@BP samples

Multi-walled carbon nanotube BP was purchased from Nanjing Jicang Material Science and Technology Co. and carbon cloth was bought from Suzhou Sinero Technology Co.. Nickel acetate and thiourea were sourced from Aladdin Reagent Co.. Before its use, the BP was soaked in absolute ethanol and acetone, followed by ultrasonic cleaning for 10 min to eliminate surface impurities. To produce the electrodes, first, a 0.1 M solution of thiourea and nickel acetate was prepared by dissolving them in a 1:1 mixture of ethanol and water, which was then magnetically stirred until complete dissolution of the Ni and S precursors. Subsequently, the solution was dropped onto the BP at a concentration of 333 μL cm^{-2} and left to dry in the air.

In the rapid Joule heating device with a vacuum environment (HTS-7026D from Shenzhen Joule IC Technology Co.), the BP-based precursor was directly clamped on the sample stage. The synthesis temperature was adjusted by controlling the thermal shock voltage. Samples were prepared at different temperatures, 1300 K, 1400 K, and 1500 K, and denoted as Ni_3S_2-NiO@BP-1300, Ni_3S_2-NiO@BP-1400, and Ni_3S_2-NiO@BP-1500, respectively. The final mass of active material was determined to be approximately 2 mg cm^{-2} by measuring the weight of the BP before and after the metal loading.

2.2. Materials characterization

The morphology and internal structure of the samples were characterized using scanning electron microscopy (SEM, Quanta FEG 250) and transmission electron microscopy (TEM, JEOL jem-2100f). X-ray diffraction (XRD) patterns of the obtained product were collected using a Rigaku D/max 2500 diffractometer with Cu-K-α radiation (λ = 1.54178 Å) in the range of 100 ~ 80 (2θ) and a step size of 0.020. X-ray photoelectron spectroscopy (XPS) analysis was performed on a Thermo ESCALAB 250. Raman spectroscopic characterization was carried out using a LabRAM HR800 spectrometer (HORIBA Jobin Yvon Corporation).

2.3. Electrochemical tests

The electrochemical properties of the prepared materials including cycling voltammetry (CV), galvanostatic charge–discharge (GCD), and electrochemical impedance spectroscopy (EIS) in the frequency range between 100 kHz and 0.01 Hz were conducted using a three-electrode system by CHI 760E electrochemical workstation (Shanghai Chenhua Instrument Corp., China) and cycling stability was performed using a Neware CT-4008 battery test kit. The three-electrode setup consisted of Ni_3S_2-NiO@BP directly as the working electrode, Hg/HgO as the reference electrode, Pt foil as the counter electrode, and 6 M KOH as the electrolyte. In the two-electrode system, the asymmetric supercapacitor (ASC) was fabricated with Ni_3S_2-NiO@BP-1400 and active carbon (AC) as the electrodes, glass filter paper as the separator, and a 3 M KOH solution as the electrolyte. For the preparation of the AC electrode, acetylene black and polyvinylidene fluoride were mixed in a mass ratio of 8:1:1, and an appropriate amount of n-methylpyrrolidone was added to form a uniform slurry. The slurry was evenly coated on the cleaned carbon cloth and dried in vacuum at 60 °C for 24 h. The mass ratio of Ni_3S_2-NiO@BP to AC was determined using the calculation $m^+C^+\Delta V^+ = m^-C^-\Delta V^-$, where m (g), C (F g^{-1}), and ΔV (V) represent the mass, the specific capacitance, and the potential window of the positive (Ni_3S_2 −NiO@BP) and negative (AC) electrodes. The flexible two-electrode device uses polyethylene terephthalate as the outer shell and a nickel sheet as the electrode ear. According to the GCD measurements, the specific capacitance of as-made samples and the hybrid supercapacitor were calculated using the equation:

$$c = \frac{i\Delta t}{m\Delta V} \tag{1}$$

in which i represents the discharge current (A), Δt is the discharge time (s) and ΔV is the potential window. The mass of active material in a single electrode was approximately 2 mg. The energy density (E, Wh kg^{-1}) and power density (P, W kg^{-1}) of the hybrid supercapacitor were determined by the following formulas:

$$E = \frac{C\Delta V^2}{2} \tag{2}$$

$$P = \frac{3600E}{\Delta t} \tag{3}$$

2.4. Computational method

Spin-polarized density functional theory (DFT) calculations were performed by using the Vienna ab initio simulation package (VASP) [21]. The generalized gradient approximation (GGA) of the Perdew-Burke-Ernzerhof (PBE) functional was employed as the exchange and correlation functional [22,23]. The projector-augmented wave (PAW) method was used to describe the electronic structure with a cutoff energy of 500 eV [24]. The 4 × 4 × 1 Monkhorst–Pack k-point mesh was applied to sample the Brillouin zone for all structures [25]. All atoms were allowed to relax until the forces converged to less than 0.015 eV $Å^{-1}$ and the energy change dropped below 1×10^{-6} eV. A vacuum region of 15 Å was introduced along the z-axis for all samples to eliminate the potential interaction between the model and its mirror image.

The three-layer slab models of Ni_3S_2(1 1 1) and NiO(1 1 1) were chosen to represent pristine Ni_3S_2 and NiO, respectively. A composite model comprising two layers of NiO and two layers of Ni_3S_2 was designed for the Ni_3S_2-NiO(1 1 1) heterostructure. The adsorption energy (E_{ads}) of OH^- on the sample was calculated according to the equation:

$$E_{ads} = E_{sample+OH^-} - E_{OH^-} - E_{sample} \tag{4}$$

where $E_{sample+OH^-}$, E_{OH^-}, $and E_{sample}$ represent the total energy of the samples after the OH^- adsorption, the energy of free OH^- , and the energy of clean NiO(1 1 1), Ni_3S_2(1 1 1), or Ni_3S_2-NiO(1 1 1) heterostructure, respectively.

3. Results and discussions

3.1. Characterization

Fig. 1**a** schematically shows the process of producing Ni_3S_2-NiO@BP electrodes from the soaking of BP with thiourea and nickel acetate and their posterior thermal shock processing in vacuum. The surface of the

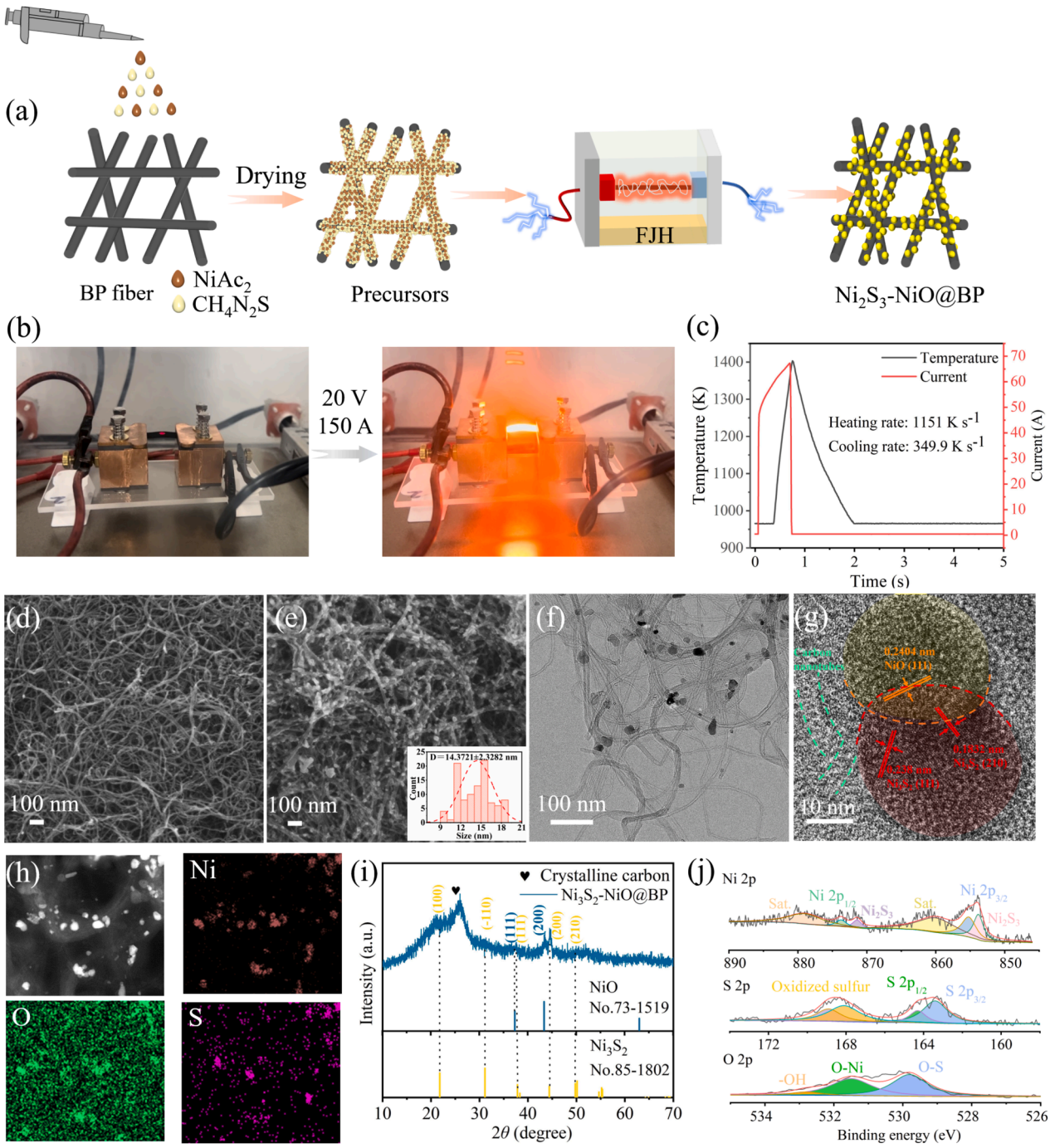

Fig. 1. (a) Schematic diagram of the process of preparation of Ni_3S_2-NiO@BP; (b) Optical images of the Ni_3S_2-NiO@BP before and during the Joule-heating synthesis process; (c) Temperature evolution during the 0.6 s of the thermal shock; (d) SEM image of the pristine BP; (e) SEM image of Ni_3S_2-NiO@BP; (f) TEM and (g) HR-TEM images of Ni_3S_2-NiO@BP; (h) EDS elemental mapping of Ni_3S_2-NiO@BP; (i) XRD pattern and (j) XPS spectra of Ni_3S_2-NiO@BP.

carbon nanotubes (CNTs) of the BP is first covered with a layer of thiourea and nickel acetate by drop coating and dried under natural conditions to obtain a carbon-based precursor, which is then in-situ rapidly reacted using a Joule heating device in a vacuum environment that eliminates the need for chemical gases. For the thermal processing, as shown in Fig. 1b, the ends of the BP are clamped through copper sheets. The synthesis temperature is controlled by adjusting the power supply. As an example, when a thermal shock voltage of 20 V was applied, the carbon-based precursor reached 1400 K in 750 ms, with an estimated heating rate of 1150 K s^{-1} and a cooling rate of 350 K s^{-1}, as illustrated in Fig. 1c. The thermal shock leads to the instantaneous decomposition of thiourea and evaporation of sulfur which reacts with Ni^{2+} ions to create nickel sulfide. Besides, NiO particles are formed by the decomposition of nickel acetate and the partial reaction of Ni^{2+} ions with oxygen traces in the vacuum ambient [26,27]. The rapid process prevents significant crystal growth and agglomeration, while also retaining the tubular structure of the BP.

Fig. 1d displays the pristine BP made of smooth carbon nanotubes with a diameter of about 20 nm. After the metal loading and the thermal processing (Fig. 1e), the BP appears filled with a large density of small particles, with no fracture of the BP or obvious aggregation of the particles observed. The particle size distribution histogram (Fig. S1)

revealed an average size of 14 ± 3 nm. As shown in Fig. S2, the size of the nanoparticles in the samples was adjusted by the thermal shock temperature. The relationship between particle size and temperature was non-linear. At moderate temperatures, such as 1300 K, a moderate density of nuclei is formed, leaving a substantial amount of precursor available for particle growth. This leads to the formation of relatively large particles. At higher temperatures, nucleation is promoted, which reduces the precursor available for further particle growth. Nevertheless, at sufficiently high temperatures, particle aggregation and Ostwald ripening occur, ultimately resulting in larger particles once again.

TEM characterization (Fig. 1f) exposes the hollow structure and open architecture of the interconnected nanotubes and the homogeneous distribution and tight bonding of Ni_3S_2-NiO heterostructures with the carbon nanotube backbone. High-resolution TEM (HRTEM) analysis (Fig. 1g) shows lattice spacings of the nanoparticles at 0.2404, 0.1832, and 0.238 nm, corresponding to the (1 1 1) plane of NiO and the (2 1 0) and (1 1 1) crystal planes of Ni_3S_2, respectively. Notably, the tight lattice connection between Ni_3S_2 and NiO indicates the formation of heterostructure interface, which synergistically combines their properties, introducing a charge modulation effect and accelerating charge carrier transport by generating internal electric fields. The EDS results of the Ni_3S_2-NiO@BP composite in Fig. 1h and Fig. S3 confirm the presence of Ni, O, and S on the surface of the CNTs. As shown in Fig. 1h, the concentrations of Ni and S elements are relatively higher in some regions, indicating that the Ni_3S_2 particles are unevenly distributed on the BP substrate, likely due to localized aggregation during the rapid thermal shock process. In contrast, O is more uniformly distributed throughout the sample, which correspond to the homologous origin of Ni and O from nickel acetate. Additionally, the 3D network structure of the BP substrate may cause variations in nanoparticle adherence during synthesis, further contributing to the uneven distribution.

The XRD pattern in Fig. 1i shows several sets of diffraction peaks. A first set at 37.33° and 43.38° is associated with the (1 1 1) and (2 0 0) planes of NiO. A second set at 21.75°, 31.10°, 37.80°, 44.35°, and 50.11° is assigned to the (100), ($\bar{1}$10), (1 1 1), (2 0 0), and (2 1 0) planes of the Ni_3S_2 phase. Besides the characteristic broad band at about 21° belongs to the amorphous carbon peak of BP, and a sharp diffraction peak near 26.15° for the sample after thermal shock proves the presence of crystalline graphitic carbon, revealing that the Joule heating process enhances the BP crystallinity. The Raman spectra of the different samples (Fig. S4) display two characteristic peaks at 1351 cm^{-1} and 1598 cm^{-1}, corresponding to the characteristic defective (D) and graphitic (G) bands of carbon, respectively. The intensity ratio between D and G bands (I_D/I_G) for the pristine BP is 1.103, and it decreases to 1.045, 1.006, and 1.010 after the rapid annealing at 1300 K, 1400 K, and 1500 K, respectively [28]. The lowest ratio reached at 1400 K denotes the highest degree of graphitization, similar to that obtained at 1500 K. As shown in Fig. 1j, the Ni 2p XPS spectrum of the Ni_3S_2-NiO@BP-1400 sample was fitted with two doublets at 853.8 eV and 855.3 eV (Ni $2p_{3/2}$) and the corresponding satellite peaks, assigned to Ni within Ni-S and Ni-O environments [29]. The S 2p XPS spectrum also displayed two doublets at 163.4 eV and 168.1 eV (S $2p_{3/2}$) assigned with sulfur within the metal sulfide lattice and oxidized sulfur, respectively [30]. The O 1 s XPS spectrum exhibited was deconvoluted with bands associated with Ni-O bonds at 531.5 eV, S-O bonds at 529.8 eV, and a minor amount of OH^- adsorbed on its surface [31].

3.2. Electrochemical performance in the three-electrode system

The electrochemical performances of BP and Ni_3S_2-NiO@BP electrodes was systematically evaluated in a three-electrode setup using aqueous 6 M KOH as the electrolyte. CV and GCD curves and the EIS spectra were recorded to investigate the impact of the Joule heating temperature on the electrochemical properties of materials. All samples were directly employed as working electrodes without incorporating binders or electrically conducting additives. The CV curves of the original BP, Ni_3S_2-NiO@BP-1300, Ni_3S_2-NiO@BP-1400, and Ni_3S_2-NiO@BP-1500 in the voltage interval of −0.1 V to 0.6 V vs.Hg/HgO are illustrated in Fig. 2a. The typical rectangular-like shape of the CV curve of BP in Fig. S5a suggests its double electric layer capacitive energy storage process. In contrast, the CV curves of the Joule-heated samples exhibit distinct Faraday redox peaks associated with the redox of the Ni ions during charging and discharging, underscoring its pseudocapacitance nature. Among the different electrodes, Ni_3S_2-NiO@BP-1400 exhibits the largest capacitance, and the broadest reduction peak reflects a more gradual and extended reduction process. This can be attributed to the uniform distribution of nanoparticles providing more electrochemically active sites.

The GCD curves in Fig. 2b show a charge–discharge plateau which confirms the presence of redox reactions. Fig. 2c presents the CV curves of the Ni_3S_2-NiO@BP-1400 at scanning rates ranging from 1 to 100 mV s^{-1}. At low scan rates, the area of the CV curves increases as the scan rate rises, which is attributed to charge storage being predominantly diffusion-controlled at low scan rates, allowing ions sufficient time to reach active sites and produce larger capacitance. However, as the scan rate continues to increase, the CV area change becomes less pronounced. This is because the charge storage mechanism transitions from diffusion-controlled to surface-controlled processes, where Faradaic reactions primarily occur on or near the surface of the nanoparticles. Additionally, the fast charge–discharge behavior at high scan rates minimizes the contribution of the slower diffusion-controlled redox reactions, resulting in the disappearance of the oxidation peak. The notable alteration in redox peak potential with increasing scanning rate may be attributed to increased resistance between the electrolyte and the active electrode [32]. GCD curves at various current densities (Fig. 2d) display clear charge/discharge plateaus that confirm the pseudocapacitance, a rapid charging/discharging capacity, and an excellent Coulomb efficiency [33–35]. The specific capacitance of Ni_3S_2-NiO@BP-1400 is calculated to reach 2278F g^{-1} at 1 A g^{-1}, and it remains 1080F g^{-1} even at 10 A g^{-1}, demonstrating its excellent high-rate performance. The GCD curve of BP in Fig. S5b shows a symmetrical triangular shape with a capacity of 3.2F g^{-1} at a current density of 1 A g^{-1}, which can be neglected compared with those of the Ni-containing electrodes. The specific capacitance data for the samples at various current densities are presented in Fig. 2e. Notably, the specific capacitance of Ni_3S_2-NiO@BP-1400 at 1 A g^{-1} surpasses its counterparts Ni_3S_2-NiO@BP-1300 (1698F g^{-1}) and Ni_3S_2-NiO@BP-1500 (1430F g^{-1}). Even at a higher current density of 5 A g^{-1}, Ni_3S_2-NiO@BP-1400 retains a remarkable 67 % of its initial capacitance, while Ni_3S_2-NiO@BP-1300 and Ni_3S_2-NiO@BP-1500 retain only 12 % and 13 %, respectively. These results highlight the impact of thermal shock temperature on the structure of Ni_3S_2-NiO and its energy storage performance, consistent with CV analysis [36,37].

To further analyze the energy storage mechanism of Ni_3S_2-NiO@BP-1400, capacitance-controlled and diffusion-controlled contributions were quantified using Dunn's method with CV curves at slow scan rates. The current response (i) was separated into capacitance-controlled (k_1v) and diffusion-controlled ($k_2v^{1/2}$) contributions, expressed as $i = k_1v + k_2v^{1/2}$. The CV profiles of the samples at 5 mV s^{-1} are depicted in Fig. 2f, where the blue region represents the capacitive contribution. The diffusion-controlled contribution on the Ni_3S_2-NiO@BP-1400 approaches nearly 20 %, underscoring its role in the total capacitance of the battery-like capacitor electrode [38]. Fig. 2g demonstrates the distribution of capacity between diffusion-controlled and capacitance-controlled processes at varying scan speeds, with the capacitance contribution escalating from 49 % to 80 % as the scan rate increases from 1 mV s^{-1} to 5 mV s^{-1}. The ultrarapid Joule heating process allows for inhibiting particle growth, retaining a small particle size of nickel sulfide and nickel oxide, enlarging the exposed area, and shortening ion diffusion path length, which is primarily manifested by the contribution of the capacitance-controlled procedure. Comparisons with other investigations reveal that the Ni_3S_2-NiO@BP-1400 composites prepared

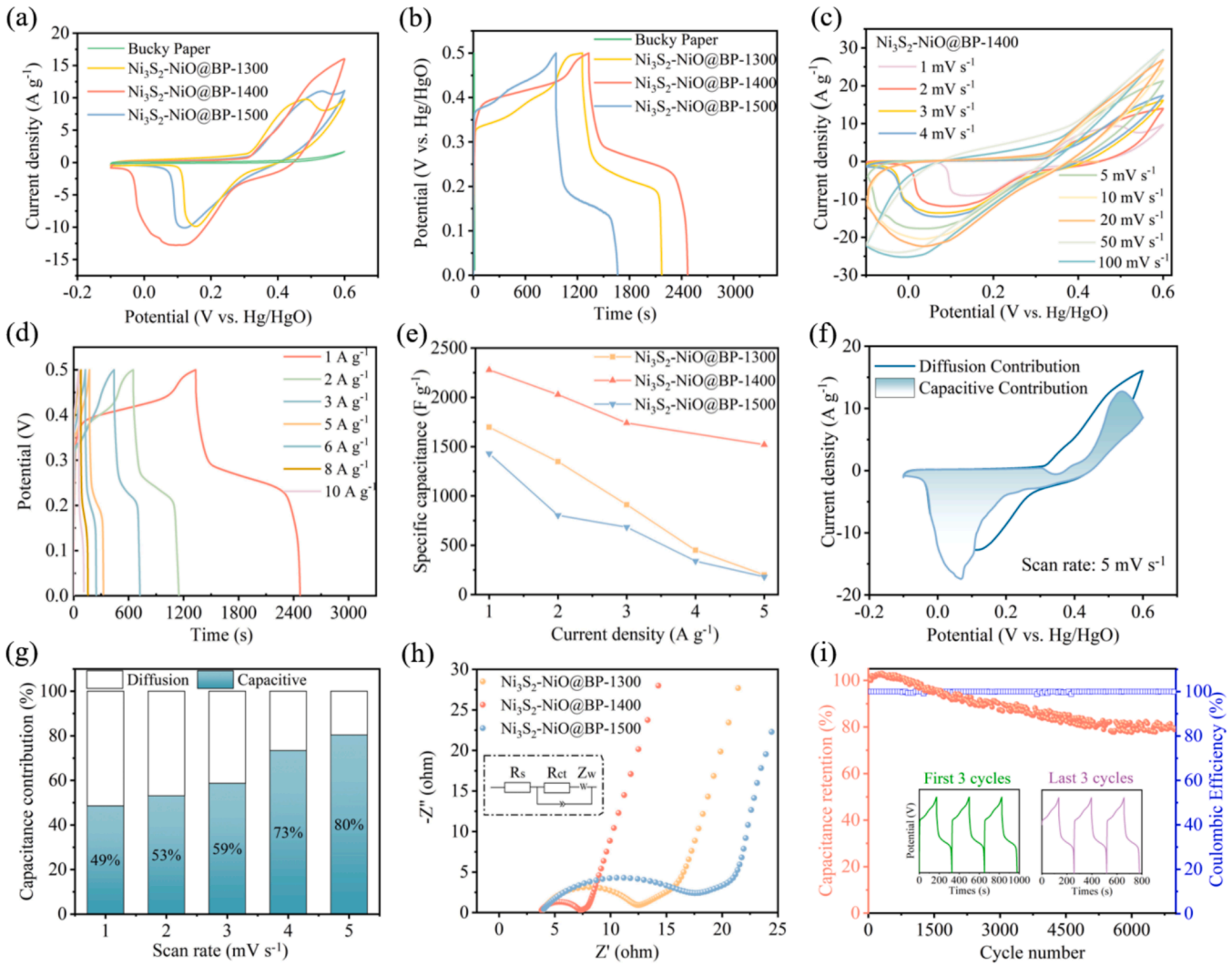

Fig. 2. (a,b) CV (a) and GCD (b) curves of BP and Ni_3S_2-NiO@BP samples obtained at different heating temperatures; (c) CV curves of Ni_3S_2-NiO@BP-1400 at different sweep rates; (d) GCD curves of sample Ni_3S_2-NiO@BP-1400 at different current densities; (e) Corresponding specific capacitance calculated based on the GCD results of Ni_3S_2-NiO@BP samples at 1–5 A g^{-1}; (f) Separation of current contribution at 5 mV s^{-1}; (g) Contribution diffusion controlled capacities at slow scan rates; (h) Nyquist plots of Ni_3S_2-NiO@BP samples and the chosen equivalent circuit; (i) Cycle performance and coulombic efficiency of Ni_3S_2-NiO@BP-1400 at a current density of 5 A g^{-1}.

by the Joule heating method possess excellent capacity and are better than most of the previously reported results, as shown in Table S2. It is worth mentioning that the prepared Ni_3S_2-NiO@BP electrode not only exhibits better capacitance performance, but its preparation method is more energy-efficient.

To elucidate the reaction kinetics and conductivity of the electrodes, Fig. 2h presents the Nyquist plots of the samples obtained at different heating temperatures. The equivalent circuit model inset in Fig. 2h aids in fitting the Nyquist curves to determine intrinsic ohmic resistance (R_s), originating from the electrolyte ionic resistance and electrode resistance, and the charge transfer resistance (R_{ct}). Fitting results in Table S3 show a R_s value of 3.8 Ω for Ni_3S_2-NiO@BP-1400, which is very similar to that of Ni_3S_2-NiO@BP-1500 (3.7 Ω) and Ni_3S_2-NiO@BP-1300 (3.9 Ω). In contrast, a significantly lower R_{ct} value of 3.4 Ω was obtained for Ni_3S_2-NiO@BP-1400, compared with Ni_3S_2-NiO@BP-1300 (8.0 Ω) and Ni_3S_2-NiO@BP-1500 (12.9 Ω), indicating that Ni_3S_2-NiO@BP-1400 exhibited superior charge transfer capability compared the other samples. This can be attributed to the optimized graphitization of the BP substrate enhancing conductivity, the smallest and most uniformly distributed nanoparticles increasing the electrochemical active surface area and reducing ion diffusion resistance. The straight lines observed in the low-frequency region of the Nyquist plots depict the ion diffusion resistance from the electrolyte solution to the electrode interface. Notably, all samples display straight lines with an inclination angle greater than 45 degrees, indicating favorable electrolyte ion transport. The stability of the Ni_3S_2-NiO@BP-1400 electrode was analyzed through 7000 consecutive charge–discharge cycles at 5 A g^{-1}, as reflected in Fig. 2i. The electrode exhibites notable cycling stability, with the capacity consistently increasing during the pre-activation phase, as electrolyte ions gradually penetrate deep into the electrode structure and activate additional electrochemical sites, reaching 1000 cycles with a 100 % capacity retention [39]. Subsequently, the capacitance decreased to 90 % of the initial value between 1000 and 3000 cycles and to 80 % by 7000 cycles. The minimal variation observed between the initial three cycles and the last three cycles of the GCD curves in the inset of Fig. 2i further indicates the excellent electrochemical stability of the electrode. Fig. S6 presents the SEM images of the Ni_3S_2-NiO@BP-1400 electrode after cycling. In Fig. S6a, partial damage to carbon nanotubes can be observed, likely caused by mechanical vibrations during long-term cycling, while the overall framework of the BP substrate remains intact (Fig. S6b). Additionally, nanoparticle aggregation and detachment are evident, reducing the utilization of active materials and

contributing to the decline in electrochemical performance during cycling. EDS results after cycling (Table S4) reveal significant sulfur loss from the Ni_3S_2 phase, reducing active redox sites and causing performance decline. Overall, these results indicate that the Ni_3S_2-NiO@BP electrodes possess favorable cycling stability and can be considered a promising candidate for supercapacitor applications.

3.3. Energy storage mechanism analysis

To gain deeper insights into their energy storage mechanism, ex-situ XRD and Raman spectroscopy analyses were carried out during the charge and discharge of the device, as shown in Fig. 3**a**. The characteristic XRD peaks of Ni_3S_2 gradually disappear as the voltage increases, while the characteristic diffraction peaks of $Ni(OH)_2$ (PDF#14-0117) at 25.95° and 37.93°, and NiOOH (PDF#06–0075) at 33.06° and 62.73° were detected. This suggests that at the early stages of charging, Ni_3S_2 reacts with OH^- in the electrolyte to form NiOOH. Combined with the Raman spectra shown in Fig. 3c, the pronounced peak at 518 cm^{-1} attributed to the Ni-O stretching mode of NiO disappears as the voltage rises further to 0.5 V, indicating the complete conversion to NiOOH [40]. The XRD results confirm this transformation, as the diffraction peaks of NiO and Ni_3S_2 gradually disappear with increasing voltage. Both XRD and Raman results during the discharge process reveal that NiOOH is reduced back to $Ni(OH)_2$, NiO, and Ni_3S_2, releasing the stored energy. No new peaks appeared during the charge and discharge process, indicating that no new phase was formed. However, due to the slower reduction rate compared to oxidation, the reduction process is not fully completed when the voltage drops to 0 V [41]. As the cycle proceeds, NiOOH could be completely converted to Ni_3S_2-NiO during the fast charge–discharge process [42]. The analysis indicates that the charge storage and release mechanisms are primarily governed by the redox reactions involving Ni^{2+} and Ni^{3+} ions. The reactions can be summarized as follows [43,44]:

$$Ni_3S_2 + 3OH^- \leftrightarrow Ni_3S_2(OH)_3 + 3e^-(5)$$

$$Ni_3S_2(OH)_3 + OH^- + e^- \leftrightarrow NiOOH + H_2O + S^{2-}(6)$$

$$NiO + OH^- + H_2O \leftrightarrow Ni(OH)_2 + e^-(7)$$

$$Ni(OH)_2 + OH^- \leftrightarrow NiOOH + H_2O + e^-(8)$$

The above results verify the mutual conversion of Ni_3S_2 and NiO with hydroxide and hydroxyl oxide respectively when Ni_3S_2-NiO@BP undergoes electrochemical reactions in alkaline electrolyte. Based on the above structural and capacitive performance characterization, the structural evolution of the electrode during charge and discharge is illustrated in Fig. 3d.

Furthermore, DFT calculations were conducted comparatively for pristine NiO(1 1 1), Ni_3S_2(1 1 1), and Ni_3S_2-NiO(1 1 1) heterostructure to analyze their performance enhancement mechanism. As illustrated in Fig. 4**a**, the top-view and side-view models of OH^- adsorption on the samples were established and optimized to simulate the participation of an alkaline electrolyte in the electrochemical reaction. Fig. 4b shows that the OH^- adsorption energy on NiO is −1.21 eV, while on Ni_3S_2 it becomes −1.38 eV. The largest adsorption energy of −2.16 eV can be determined on Ni_3S_2-NiO heterostructure, representing the most stable OH^- adsorption. The underlying reason can be explained by the partial density of states (PDOS) shown in Fig. 4c. The d-band center of Ni_3S_2-NiO (−1.86 eV) shifts closer to the Fermi level than that of NiO (−2.23 eV) and Ni_3S_2 (−2.04 eV), indicating that the Fermi level on the Ni_3S_2-NiO surface more readily facilitates the adsorption process. Furthermore, the upward shift of the d-band enhances electron conductivity,

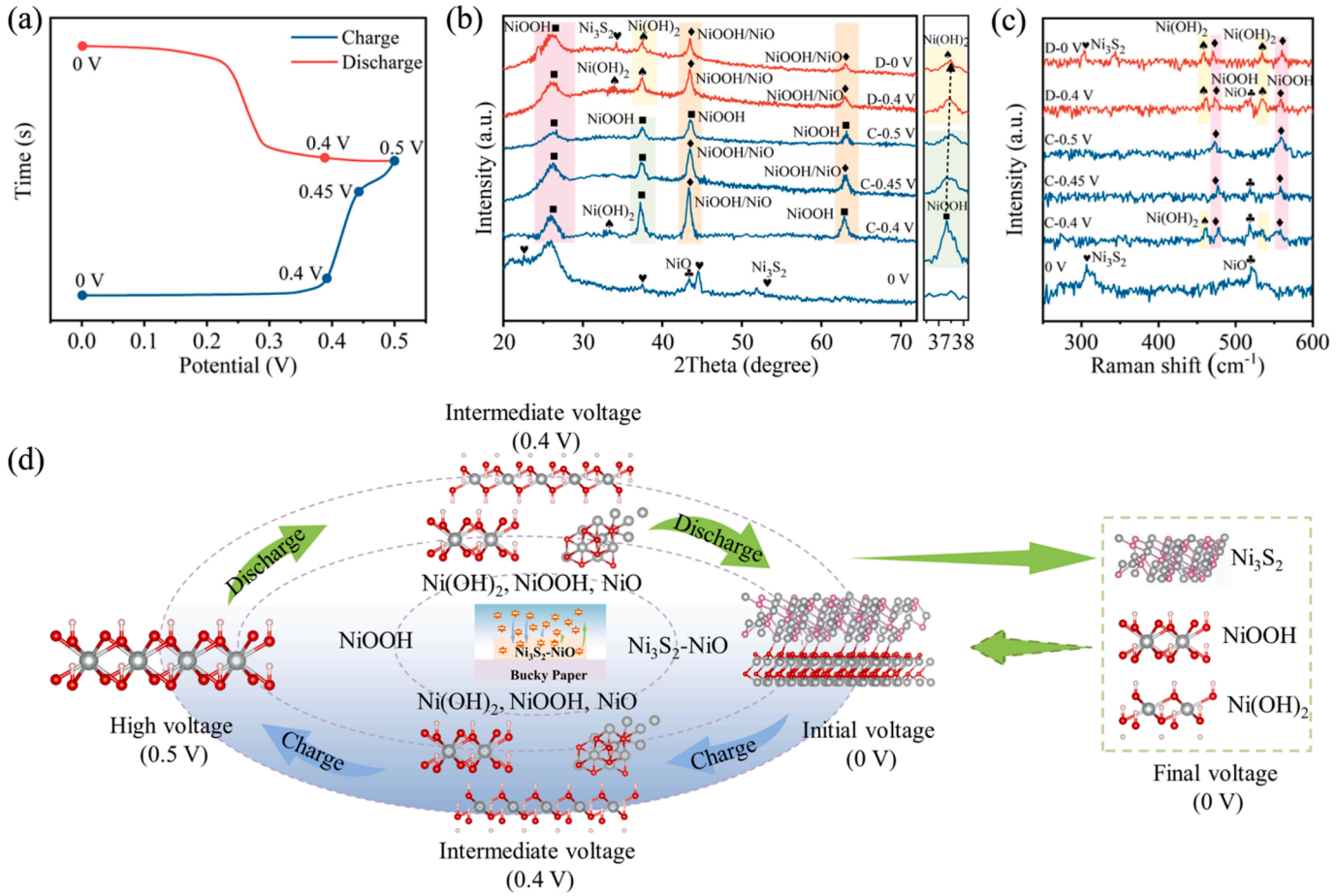

Fig. 3. (a) GCD curves of Ni_3S_2-NiO@BP at a current density of 1 A g^{-1}; (b) XRD patterns and (c) Raman spectra of Ni_3S_2-NiO@BP obtained from different potentials during charge and discharge process; (d) Schematic diagram of the structural evolution of Ni_3S_2-NiO during charge and discharge.

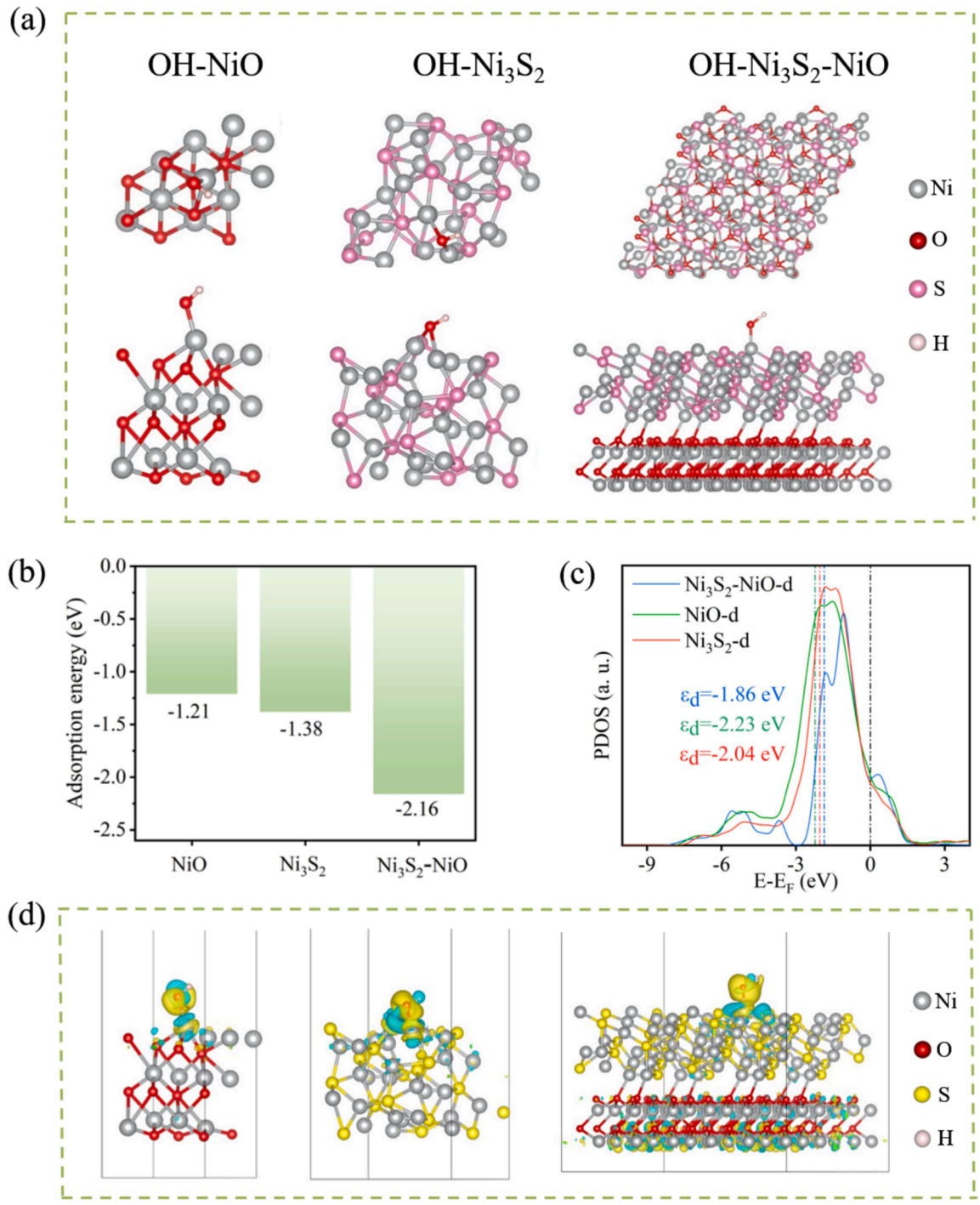

Fig. 4. (a) Top-view (upper) and side-view (lower) models of OH^- adsorption on optimized pristine NiO (1 1 1), Ni_3S_2 (1 1 1), and Ni_3S_2-NiO (1 1 1) heterostructure, respectively. The grey, pink, red, and white spheres represent Ni, S, O, and H atoms, respectively. (b) Adsorption energy of OH^- of the above three samples. (c) Partial density of states (PDOS) of active Ni atom in pristine NiO, Ni_3S_2, and Ni_3S_2-NiO heterostructure; (d) Differential charge density of OH^- adsorbed on pristine NiO, Ni_3S_2, and Ni_3S_2-NiO heterostructure. Yellow and cyan regions represent electron accumulation and depletion, respectively. (For interpretation of the references to colour in this figure legend, the reader is referred to the web version of this article.)

which also significantly facilitates both redox activity and electron mobility [45]. This confirms that constructing a heterostructure enhances redox reaction kinetics. In addition, the differential charge density was calculated to simulate rapid charge transfer at the boundary of the heterogeneous interface, as shown in Fig. 4d. Dissipating electron regions are highlighted in cyan, while accumulating regions are in yellow. Differential charge density analysis indicates that the electrons will transfer from the Ni atom to the OH species after OH^- adsorption on various samples. The electron interaction occurs between the p orbitals of the oxygen atom and the d orbitals of the Ni atom, with electrons hybridizing and transferring between the two orbitals, leading to a redistribution of the electron density distribution around the Ni atom. Due to the electronic interaction at the Ni_3S_2 and NiO heterogeneous interface, the Ni_3S_2-NiO structure exhibits a richer electronic state, where the largest electron accumulation around OH species is observed, consistent with the highest adsorption energy. These calculations

further verify that the construction of the heterostructure benefits the enhancement of redox reaction kinetics, in agreement with the electrochemical experimental results.

3.4. Device application in two-electrode system

To evaluate the potential practical applications of the Ni_3S_2-NiO@BP electrode, Ni_3S_2-NiO@BP//AC HSC devices were assembled as shown schematically in Fig. 5a. Fig. 5b compares the CV curves of AC and Ni_3S_2-NiO@BP electrodes at 20 mV s^{-1} in a three-electrode system, showcasing potential windows of −1 ~ 0 V and −0.1 ~ 0.6 V, respectively. This extension allows the theoretical optimal potential window for the HSC device to extend to 1.6 V. As the operational voltage window is increased to 1.6 V, the CV curves show a sharp polarization, as shown in Fig. 5c. Therefore, CV tests of the device were performed at various sweep speeds within the voltage range of 0–1.5 V [46,47]. The obtained CV curves in Fig. 5d exhibit a clear redox peak and a rectangle-like shape, reflecting that the capacitive response of the device results from a combination of redox reactions and capacitive behavior.

The GCD curves in Fig. 5e demonstrate approximate symmetry, indicating high Coulombic efficiency and excellent electrochemical reversibility. Based on the discharge curves, the specific capacitance of the HSC is 153F g^{-1} at 1 A g^{-1} (Fig. 5f). Even at a higher current density of 10 A g^{-1}, the specific capacitance remains at 53 F g^{-1}, showcasing the excellent rate capability of the device. The power and energy densities of the HSC devices are summarized in the Ragone plot [48–53] in Fig. 5g, where the HSC can deliver an energy density of 72 Wh kg^{-1} at a power density of 1125 W kg^{-1}. This maximum energy density is comparable to or exceeds that of most previously reported transition metal sulfide-based HSC devices [54]. The cycling stability at a current density of 15 A g^{-1} is depicted in Fig. 5h, where the specific capacitance remains at 83 % of the initial value after the Ni_3S_2-NiO@BP//AC device undergoes 10,000 cycles. The Coulomb efficiency remains stable throughout the cycling process, demonstrating excellent charge–discharge reversibility of the electrode material. Additionally, the inset in Fig. 5(h) illustrates the slight variation in the charging and discharging times of the HSC device during the initial and the last several cycles further indicating superior cycling stability.

As illustrated in Fig. 6a, to confirm the flexible application performance of the material, electrochemical tests were carried out under different bending angles. The CV curves of Ni_3S_2-NiO@BP//AC HSC device performed at different bending angles (0, 60, 90, 120°) at 20 mV s^{-1} are displayed in Fig. 6b. The results indicate that the shape of the CV curve presents almost no variation, and there was negligible loss of capacity upon bending, thus confirming its good flexibility and excellent stability [55]. Further validation of its capabilities is demonstrated in Fig. 6c where the electronic watch remained illuminated for more than 30 min, showcasing the impressive energy storage performance of the Ni_3S_2-NiO@BP//AC HSC. To showcase its applicability, after being charged, the flexible device was attached to a wristband and utilized as a

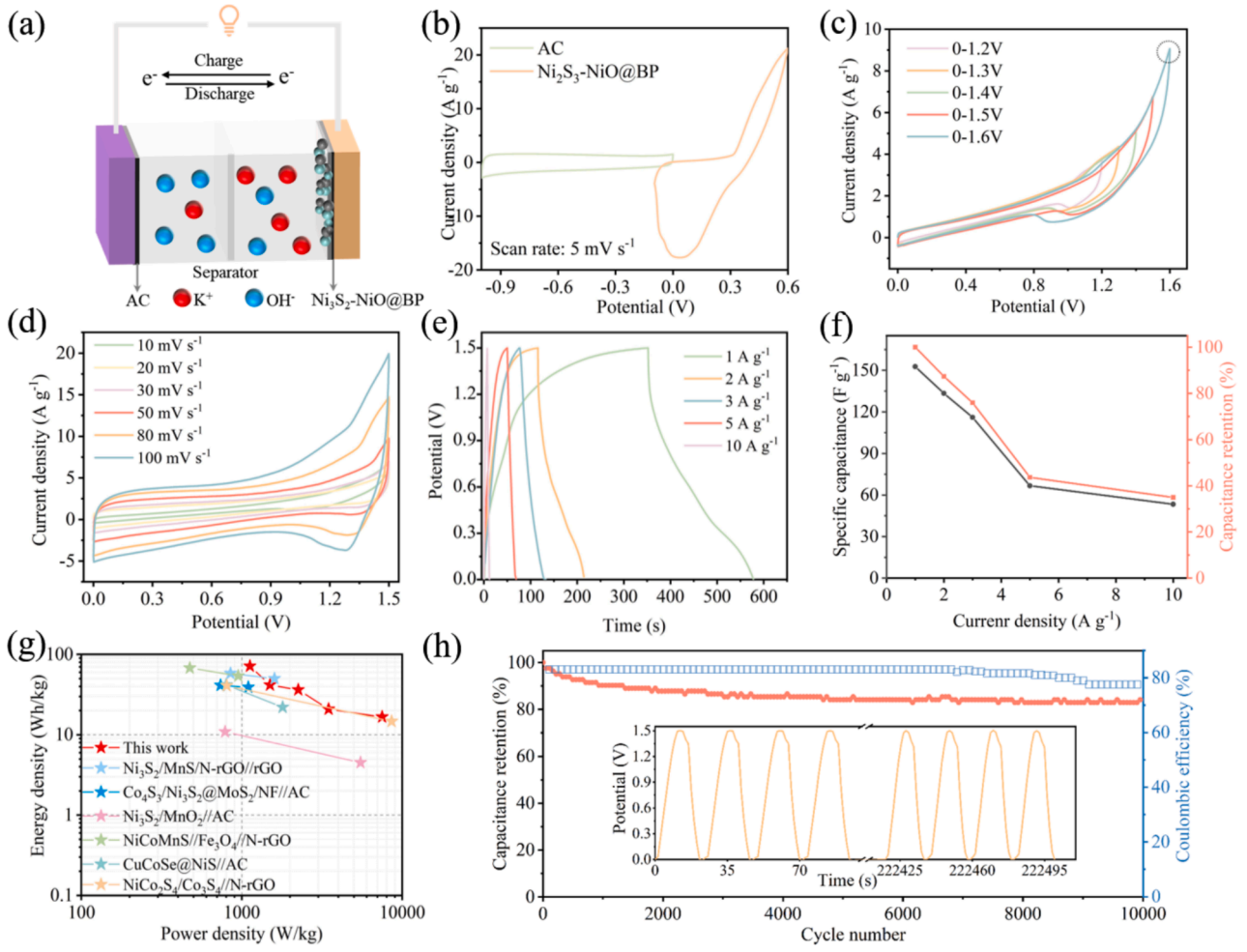

Fig. 5. (a) Schematic diagram of the as-fabricated Ni_3S_2-NiO@BP//AC HSC device; (b) comparative CV curves of Ni_3S_2-NiO@BP and AC electrodes performed in a three-electrode configuration; (c) CV curves of the HSC device in different operation windows scanned at a scan rate of 10 mV s^{-1}; (d) CV curves of the HSC device at different sweep rates; (e) GCD graphs of the HSC device at different current densities; (f) Study of specific capacities with current density; (g) Ragone plots; (h) Cycling performance of the Ni_3S_2-NiO@BP//AC device.

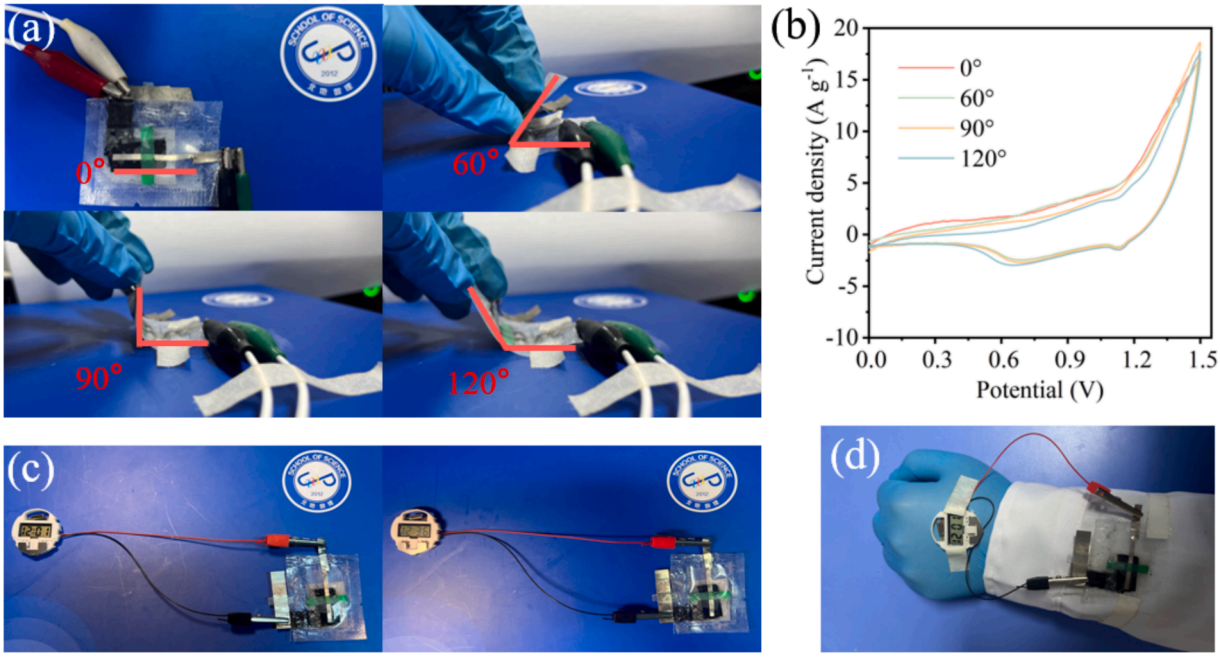

Fig. 6. (a) Photographs of Ni_3S_2-NiO@BP//AC HSC device under different bending angles; (b) CV curves of the device under various deformations at a scan rate of 20 mV s^{-1}; (c) Photographs of a lighted electronic watch powered by HSC for at least 30 min; (d) Photograph of wearable function demonstration.

flexible energy device to power an electronic watch, as depicted in Fig. 6d. Overall, these results demonstrate the flexible energy storage device exhibited excellent mechanical stability and significant potential for integration into a diverse range of wearable devices.

4. Conclusions

In the present work, we have demonstrated the successful synthesis of Ni_3S_2-NiO composites on BP using an innovative Joule heating method. This approach has proven to be both efficient and effective, offering a rapid synthesis route that eliminates the need for organic solvents, thus enhancing the sustainability of the process. By leveraging the exceptional properties of BP as a substrate, the prepared composites maintained the structure of multi-walled carbon nanotubes and achieved a uniform dispersion of active materials, significantly boosting the rapid faradic reactions. Moreover, DFT results show that Ni_3S_2-NiO@BP exhibits the best conductivity and OH^- adsorption energy. Based on the synergistic effect between Ni_3S_2 and NiO, the Ni_3S_2-NiO heterostructure demonstrates remarkable specific capacitance and rate properties, obtaining a capacitance of 2278F g^{-1} at a current density of 1 A g^{-1}. The phase transformation of Ni_3S_2-NiO during charge and discharge in alkaline electrolyte was confirmed by ex-situ XRD and Raman spectroscopy analyses, suggesting potential reaction pathways. The materials provided abundant active sites for reversible redox reactions, leading to enhanced charge storage capacity and fast redox kinetics. The Ni_3S_2-NiO@BP//AC device has an energy density of 71.55 Wh kg^{-1} at 1124.8 W kg^{-1}. Additionally, the flexible nature of the composite electrode ensured stable electrochemical performance under mechanical deformation, making it ideal for portable and wearable electronic applications. This study provides a valuable strategy for the rapid synthesis of metal sulfides on carbon-based materials and paves the way for the development of high-performance, flexible supercapacitors that will contribute to the sustainability of the energy industry.

CRediT authorship contribution statement

Ye Tian: Writing – original draft, Methodology, Investigation, Data curation. **Shuonan Wang:** Investigation. **Ning Liu:** Methodology, Investigation, Data curation. **Qian Xue:** Methodology, Data curation. **Xueqiang Qi:** Writing – review & editing, Data curation. **Hao Liu:** Writing – review & editing, Supervision. **Andreu Cabot:** Writing – review & editing, Resources. **Libing Liao:** Supervision, Resources.

Declaration of competing interest

The authors declare that they have no known competing financial interests or personal relationships that could have appeared to influence the work reported in this paper.

Acknowledgments

The work was supported by the National Natural Science Foundation of China (No.21875223),the Fundamental Research Funds for the Central Universities (No. 2652022206), the scholarship supported by the China Scholarship Council (No.202306400060-TIANYE) and High-performance Computing Platform of China University of Geosciences Beijing.

Appendix A. Supplementary data

Supplementary data to this article can be found online at https://doi.org/10.1016/j.cej.2025.160765.

Data availability

Data will be made available on request.

References

[1] J. Zhang, M. Gu, X. Chen, Supercapacitors for renewable energy applications: A review, Micro Nano Eng. 21 (2023) 100229, https://doi.org/10.1016/j.mne.2023.100229.
[2] M. Girirajan, A.K. Bojarajan, I.N. Pulidindi, K.N. Hui, S. Sangaraju, An insight into the nanoarchitecture of electrode materials on the performance of supercapacitors, Coord. Chem. Rev. 518 (2024) 216080, https://doi.org/10.1016/j.ccr.2024.216080.
[3] V. Molahalli, M.K. Singh, M. Agrawal, S.G. Krishnan, G. Hegde, Past decade of supercapacitor research-Lessons learned for future innovations, J. Energy Storage 70 (2023) 108062, https://doi.org/10.1016/j.est.2023.108062.

[4] J. Zhou, Z. Zhu, W. Shi, X. Shi, Z. Zheng, Y. Xiong, Y. Zhu, Design strategies and recent advancements of solid-state supercapacitor operating in wide temperature range, Carbon Energy 6 (2024) e504.
[5] A. Amiri, A. Bruno, A.A. Polycarpou, Configuration-dependent stretchable all-solid-state supercapacitors and hybrid supercapacitors, Carbon Energy 5 (2023) e320.
[6] R. Zhang, Z. Xu, Z. Hao, Z. Meng, X. Hao, H. Tian, Research advances of metal fluoride for energy conversion and storage, Carbon Energy (2024) e630.
[7] A.D. Mahapatra, S. Kumar, A. Sutradhar, S. Susmita, S. Sahoo, A. Misra, ZnO/CdS based high performance broadband photo-chargeable flexible supercapacitor, Electrochim. Acta 474 (2024) 143507, https://doi.org/10.1016/j.electacta.2023.143507.
[8] N. Liu, Y. Tian, L.F. Mei, Y.Y. Zhang, Z.J. Peng, Internal and external cultivation strategy toward efficient electrochemical oxygen evolution in cobalt pentlandite, ACS Sustain. Chem. Eng. 11 (2023) 16249–16265, https://doi.org/10.1021/acssuschemeng.3c04524.
[9] A. Pramanik, S. Sengupta, S.K. Saju, S. Chattopadhyay, M. Kundu, P.M. Ajayan, Ternary metal sulfides as electrode materials for Na/K-Ion batteries and electrochemical supercapacitor: advances/challenges and prospects, Adv. Energy Mater. 14 (2024) 2401657, https://doi.org/10.1002/aenm.202401657.
[10] J. Zhao, H. Yang, S. Dong, Y. Wang, X. Lv, Q. Zhang, L. Wen, Fe-Co-S nanoarrays on nickel foam as binder-free electrodes for energy storage and electrocatalysis, Chem. Eng. J. 494 (2024) 152808, https://doi.org/10.1016/j.cej.2024.152808.
[11] J. Guo, H. Zhao, Z. Yang, L. Wang, A. Wang, J. Zhang, L. Ding, L. Wang, H. Liu, X. Yu, Bimetallic sulfides with vacancy modulation exhibit enhanced electrochemical performance, Adv. Funct. Mater. 34 (2024) 2315714, https://doi.org/10.1002/adfm.202315714.
[12] J. Guo, H. Zhao, Z. Yang, Y. Wang, X. Liu, L. Wang, Z. Zhao, A. Wang, L. Ding, H. Liu, Hierarchical porous 3D Ni_3N-CoN/NC heterojunction nanosheets with nitrogen vacancies for high-performance flexible supercapacitor, Nano Energy 116 (2023) 108763, https://doi.org/10.1016/j.nanoen.2023.108763.
[13] J.S. Sanchez, Z.Y. Xia, N. Patil, R. Grieco, J.H. Sun, U. Klement, R. Qiu, M. Christian, F. Liscio, V. Morandi, R. Marcilla, V. Palermo, Engineering nanostructured electrode materials for supercapacitor applications, Small 18 (2022) 2106403, https://doi.org/10.1002/smll.202106403.
[14] Q. Yin, H.B. Jia, G.G. Liu, L.Q.M. Ji, Tailoring the mechanical performance of carbon nanotubes buckypaper by aramid nanofibers towards robust and compact supercapacitor electrode, Adv. Funct. Mater. 32 (2022) 2111177, https://doi.org/10.1002/adfm.202111177.
[15] X.Y. Shan, J.Q. Zhu, P. Liu, Y. Zhong, X. Xu, X.P. He, Y.Q. Zhang, J.P. Tu, Y. Xia, C. Wang, W.J. Wan, M.H. Chen, X.Q. Liang, X.H. Xia, W.K. Zhang, Ultrafast-loaded nickel sulfide on vertical graphene enabled by joule heating for enhanced lithium metal batteries, Small 20 (2024) 2401491, https://doi.org/10.1002/smll.202401491.
[16] Q. Chen, H. Li, X. Lou, J.L. Zhang, G.G. Hou, J. Lu, Y.P. Tang, Surface oxygen coordination of hydrogen bond chemistry for aqueous ammonium ion hybrid supercapacitor, Adv. Funct. Mater. 33 (2023) 2214920, https://doi.org/10.1002/adfm.202214920.
[17] Y.G. Yao, Z.N. Huang, P.F. Xie, S.D. Lacey, R.J.J. Jacob, H. Xie, F.J. Chen, A.M. Nie, T.C. Pu, L.B. Hu, Carbothermal shock synthesis of high-entropy-alloy nanoparticles, Science 359 (2018) 1489–1494, https://doi.org/10.1126/science.aan5412.
[18] M. Rani, M. Sharma, S. Sehrawat, B.P. Singh, Recent advancement and challenges in multifunctional carbon nanotube buckypaper and its composites for energy storage and conversion applications, J. Energy Storage 73 (2023) 109063, https://doi.org/10.1016/j.est.2023.109063.
[19] R.H. Juang, J.S. Guo, Y.J. Huang, I.W.P. Chen, Experimental and theoretical investigations of covalent functionalization of 1D/2D carbon-based buckypaper via aryl diazonium chemistry for high-performance energy storage, Carbon 205 (2023) 402–410, https://doi.org/10.1016/j.carbon.2023.01.051.
[20] H.Q. Hao, R. Tan, C.C. Ye, C.T.J. Low, Carbon-coated current collectors in lithium-ion batteries and supercapacitors: Materials, manufacture and applications, Carbon Energy 6 (2024) e604.
[21] W. Kohn, L.J. Sham, Self-consistent equations including exchange and correlation effects, PhysRev.1 140 (1965) A1133–A1138, https://doi.org/10.1103/PhysRev.140.A1133.
[22] J.P. Perdew, K. Burke, M. Ernzerhof, Generalized gradient approximation made simple, PhysRevLett.7 77 (1996) 3865–3868, https://doi.org/10.1103/PhysRevLett.77.3865.
[23] B. Hammer, L.B. Hansen, J.K. Norskov, Improved adsorption energetics within density-functional theory using revised Perdew-Burke-Ernzerhof functionals, PhysRevB 59 (1999) 7413–7421, https://doi.org/10.1103/PhysRevB.59.7413.
[24] P.E. Blochl, Projector augmented-wave method, PhysRevB 50 (1994) 17953–17979, https://doi.org/10.1103/PhysRevB.50.17953.
[25] H.J. Monkhorst, J.D. Pack, Special points for Brillouin-zone integrations, PhysRevB 13 (1976) 5188–5192, https://doi.org/10.1103/PhysRevB.13.5188.
[26] S.P. Wang, Q.C. Liu, S.K. Li, F.Z. Huang, H. Zhang, Joule-heating-driven synthesis of a honeycomb-like porous carbon nanofiber/high entropy alloy composite as an ultralightweight electromagnetic wave absorber, ACS Nano 18 (2024) 5040–5055, https://doi.org/10.1021/acsnano.3c11408.
[27] R.L. Bian, D. Song, W.P. Si, T. Zhang, Y.X. Zhang, P.Y. Lu, F. Hou, J. Liang, Carbon nanotubes@nickel cobalt sulfide nanosheets for high-performance supercapacitors, ChemElectroChem 7 (2020) 3663–3675, https://doi.org/10.1002/celc.202000989.
[28] R.C. Li, P.Y. Kuang, L.X. Wang, H.L. Tang, J.G. Yu, Engineering 2D NiO/Ni_3S_2 heterointerface electrocatalyst for highly efficient hydrogen production coupled with benzyl alcohol oxidation, Chem. Eng. J. 431 (2022) 134137, https://doi.org/10.1016/j.cej.2021.134137.
[29] Y.X. Li, X. Yu, J. Gao, Y.R. Ma, Hierarchical Ni_2P/Zn–Ni–P nanosheet array for efficient energy-saving hydrogen evolution and hydrazine oxidation, J. Mater. Chem. A 5 (2023) 2191–2203, https://doi.org/10.1039/d3ta00792e.
[30] K. Krishnamoorthy, G.K. Veerasubramani, S. Radhakrishnan, S.J. Kim, One pot hydrothermal growth of hierarchical nanostructured Ni_3S_2 on Ni foam for supercapacitor application, Chem. Eng. J. 251 (2014) 116–122, https://doi.org/10.1016/j.cej.2014.04.006.
[31] S. Nayak, A.A. Kittur, S. Nayak, B. Murgunde, Binderless nano marigold flower like structure of nickel sulfide electrode for sustainable supercapacitor energy storage applications, J. Energy Storage 62 (2023) 106963, https://doi.org/10.1016/j.est.2023.106963.
[32] D.Y. Zhang, S.Y. Gao, J.W. Zhang, J.R. Wang, W.N. She, K.J. Wang, X. Xia, B. Yang, X.X. Meng, Facile solid−phase synthesis of layered NiS/rGO nanocomposite for high-performance hybrid supercapacitor, J. Power Sources 514 (2021) 230590, https://doi.org/10.1016/j.jpowsour.2021.230590.
[33] B.G. Liu, Q. Zhang, Y.H. Huang, D. Liu, W. Pan, Y.C. Mu, X.Z. Cheng, Y.J. Qin, Bifunctional flexible fabrics with excellent joule heating and electromagnetic interference shielding performance based on copper sulfide/glass fiber composites, Nanoscale 44 (2021) 18558–18569, https://doi.org/10.1039/D1NR03550A.
[34] K. Silambarasan, J. Archana, S. Athithya, S. Harish, R.S. Ganesh, M. Navaneethan, S. Ponnusamy, C. Muthamizhchelvan, K. Hara, Y. Hayakawa, Hierarchical NiO@NiS@graphene nanocomposite as a sustainable counter electrode for Pt free dye-sensitized solar cell, Appl. Surf. Sci. 501 (2020) 144010, https://doi.org/10.1016/j.apsusc.2019.144010.
[35] R. Balu, A. Panneerselvam, J.R. Rajabathar, G. Devendrapandi, S. Subburaj, S. Anand, U.S. Veerasamy, S. Palani, Synergistic effect of echinops flower-like copper sulfide@cadmium sulfide heterostructure for high-performance all-solid-state asymmetric supercapacitor, J. Energy Storage 72 (2023) 108447, https://doi.org/10.1016/j.est.2023.108447.
[36] B. Guan, Y. Li, B.Y. Yin, K.F. Liu, D.W. Wang, H.H. Zhang, C.J. Cheng, Synthesis of hierarchical NiS microflowers for high performance asymmetric supercapacitor, Chem. Eng. J. 308 (2017) 1165–1178, https://doi.org/10.1016/j.cej.2016.10.016.
[37] D. Wu, X.B. Xie, Y.P. Ma, J.J. Zhang, C.X. Hou, X.Q. Sun, X.Q. Sun, X.Y. Yang, Y. P. Zhang, H. Kimura, W. Du, Morphology controlled hierarchical NiS/carbon hexahedrons derived from nitrilotriacetic acid-assembly strategy for high-performance hybrid supercapacitors, Chem. Eng. J. 433 (2022) 133673, https://doi.org/10.1016/j.cej.2021.133673.
[38] K. Yang, M. Lou, D.T. Zhang, C.Z. Liu, Z. Li, L.C. Wang, W.M. Chen, X.Y. Zhou, $Ti_3C_2T_x$/carbon nanotube/porous carbon film for flexible supercapacitor, Chem. Eng. J. 427 (2022) 132002, https://doi.org/10.1016/j.cej.2021.132002.
[39] C.W. Ye, L. Xu, Heteroatom-doped porous carbon derived from zeolite imidazole framework/polymer core-shell fibers as an electrode material for supercapacitor, Compos. Part B-Eng. 225 (2021) 109256, https://doi.org/10.1016/j.compositesb.2021.109256.
[40] S.G. Dai, Z.F. Zhang, J.M. Xu, W.X. Shen, Q.B. Zhang, X.G. Yang, T.T. Xu, D. Dang, H. Hu, B.T. Zhao, Y. Wang, C. Qu, J.W. Fu, X.J. Li, C.G. Hu, M.L. Liu, In situ Raman study of nickel bicarbonate for high-performance energy storage device, Nano Energy 64 (2019) 103919, https://doi.org/10.1016/j.nanoen.2019.103919.
[41] S.G. Chen, Y.H. Li, B.X. Wu, Z.X. Wu, F.J. Li, J.H. Wu, P. Liu, H.B. Li, 3D meso/macroporous Ni_3S_2@Ni composite electrode for high-performance supercapacitor, Electrochim. Acta 275 (2018) 40–49, https://doi.org/10.1016/j.electacta.2018.03.028.
[42] J.P. Zhao, Y.H. Wang, Y.D. Qian, H.L. Jin, X.Y. Tang, Z.M. Huang, J.Y. Lou, Q. C. Zhang, Y. Lei, S. Wang, Hierarchical design of cross-linked $NiCo_2S_4$ nanowires bridged NiCo-hydrocarbonate polyhedrons for high-performance asymmetric supercapacitor, Adv. Funct. Mater. 33 (2022) 2210238, https://doi.org/10.1002/adfm.202210238.
[43] B.J. Huang, J.J. Yuan, Y.C. Lu, Y.T. Zhao, X.Y. Qian, H. Xu, G.Y. He, H.Q. Chen, Hollow nanospheres comprising amorphous $NiMoS_4$ and crystalline NiS_2 for all-solid-state supercapacitors, Chem. Eng. J. 436 (2022) 135231, https://doi.org/10.1016/j.cej.2022.135231.
[44] J.X. Kang, Y.F. Xue, J. Yang, Q. Hu, Q.H. Zhang, L. Gu, A. Selloni, L.M. Liu, L. Guo, Realizing two-electron transfer in Ni$(OH)_2$ nanosheets for energy storage, J. Am. Chem. Soc. 144 (2022) 8969–8976, https://doi.org/10.1021/jacs.1c13523.
[45] X.M. Chen, N. Xin, Y.X. Li, C. Sun, L.H. Li, Y.L. Ying, W.D. Shi, Y. Liu, Novel 2D/2D $NiCo_2O_4$/$ZnCo_2O_4$@rGO/CNTs self-supporting composite electrode with high hydroxyl ion adsorption capacity for asymmetric supercapacitor, J. Mater. Sci. Technol. 127 (2022) 236–244, https://doi.org/10.1016/j.jmst.2022.04.009.
[46] J. Vigneshwaran, J. Jose, S. Thomas, A. Gagliardi, R.L. Narayan, S.P. Jose, PPy-PdO modified MXene for flexible binder-free electrodes for asymmetric supercapacitors: Insights from experimental and DFT investigations, Chem. Eng. J. 487 (2024) 150555, https://doi.org/10.1016/j.cej.2024.150555.
[47] A. Prasad, M.D. Borse, G.R. Reddy, M. Asif, S.W. Joo, G.R. Dillip, Investigation of Zn-to-Co chemometric ratio in zinc cobaltite spinel as battery-type superior redox-active electrodes for hybrid supercapacitors: Density functional theory analysis, J. Phys. Chem. C. 128 (2024) 1591–1602, https://doi.org/10.1021/acs.jpcc.3c07303.
[48] G.H. Zhang, H.C. Xuan, R. Wang, Y.Y. Guan, H.S. Li, X.H. Liang, P.D. Han, Y.C. Wu, Enhanced supercapacitive performance in Ni_3S_2/MnS composites via an ion-exchange process for supercapacitor applications, Electrochim. Acta 353 (2020) 136517, https://doi.org/10.1016/j.electacta.2020.136517.
[49] C.H. Qu, J. Cao, Y.L. Chen, M.B. Wei, H.G. Fan, X.Y. Liu, X. Li, Q. Wu, B. Feng, Y. L. Yang, In-situ growth of hierarchical trifunctional Co_4S_3/Ni_3S_2@MoS_2 core-shell nanosheet array on nickel foam for overall water splitting and supercapacitor, Int.

J. Hydrogen Energy 48 (2023) 648–661, https://doi.org/10.1016/j.ijhydene.2022.09.278.

[50] A.T. Prasannakumar, R. Rohith, J. Cherusseri, R.R. Mohan, S.J. Varma, High areal capacitance and long cycling stability in asymmetric supercapacitors using binder-free, hierarchical nanostructured Ni_3S_2/MnO_2 hybrid electrodes, J. Energy Storage 55 (2022) 105723, https://doi.org/10.1016/j.est.2022.105723.

[51] T.L. Tamang, S. Sahoo, J.J. Shim, Triple-shelled nickel-cobalt-manganese sulfides hollow spheres for advanced hybrid supercapacitors, J. Power Sources 572 (2023) 233107, https://doi.org/10.1016/j.jpowsour.2023.233107.

[52] W.R. Wu, Y. Yan, X. Wang, C.Z. Wei, T. Yang, X.F.L. Xu, Interface construction of CuCoSe@NiS based on an ultrathin nanosheet for high-performance supercapacitors, J. Mater. Chem. A 23 (2024) 13818–13829, https://doi.org/10.1039/D4TA01430H.

[53] Z.X. Jia, Y.N. Wang, J.Q. Chen, Z.J. Cao, S.G. Pan, Y. Zhou, J.W. Sun, J.W. Zhu, X. Wang, Y.S. Fu, Metal-organic frameworks derived low-crystalline $NiCo_2S_4/Co_3S_4$ nanocages with dual heterogeneous interfaces for high-performance supercapacitors, Chin. Chem. Lett. 34 (2023) 107137, https://doi.org/10.1016/j.cclet.2022.01.030.

[54] N. Liu, Z.J. Peng, Y. Tian, H.K. Liu, Y.Y. Zhang, D.V. Deyneko, L.F. Mei, Cobalt pentlandite structured $(Fe,Co,Ni)_9S_8$: Fundamental insight and evaluation of hybrid supercapacitor, Appl. Surf. Sci. 611 (2023) 155568, https://doi.org/10.1016/j.apsusc.2022.155568.

[55] L. Han, H.L. Huang, J.F. Li, X.L. Yang, M. Xu, L.K. Pan, A novel redox bromide-ion additive hydrogel electrolyte for flexible Zn-ion hybrid supercapacitors with boosted energy density and controllable zinc deposition, J. Mater. Chem. A 8 (2020) 15042–15050, https://doi.org/10.1039/D0TA03547E.